RSC Advances

ROYAL SOCIETY OF CHEMISTRY

www.rsc.org/advances

Enhanced thermoelectric performance of layered SnS crystals: the synergetic effect of temperature and carrier concentration

Bao-Zhen Sun,[a,b,c] Zuju Ma,[a] Chao He[a] and Kechen Wu,[*a]

ABSTRACT

We present a detailed theoretical study of the SnS compound, which has not been investigated in depth to date, concerning its crystal structure, electronic structure and thermoelectric property. The results of this study show that pure SnS is not a good thermoelectric material but that its *ZT* can be increased by adjusting both the temperature and carrier concentration. Further, the optimal temperatures and carrier concentrations for producing the peak *ZT* are identified. The peak *ZT* is always below unity in the low-temperature *Pnma* phase; conversely, when the crystal undergoes a displacive phase transition at 878 K, the peak *ZT* is enhanced to 1.61±0.02 at 1080 K. Additionally, the average *ZT* in the *Cmcm* phase (e.g., approximately 1.3) is significantly higher than that in the *Pnma* phase (e.g., 0.31±0.05). Therefore, the optimally doped SnS material may be highly efficient in its thermal-to-electrical energy conversion at high temperatures. We attribute the remarkable high *ZT* of doped SnS to the high sensitivity of the electrical conductivity to the carrier concentration. The results of this study describe a simple

[a] *State Key Laboratory of Structural Chemistry, Fujian Institute of Research on the Structure of Matter, Chinese Academy of Sciences, Fuzhou 350002, China. E-mail: wkc@fjirsm.ac.cn; Fax: +86 591 83792932; Tel.: +86 591 83792600*

[b] *School of Chemistry and Chemical Engineering, Guangxi University, Nanning 530004, China.*

[c] *Key Laboratory of Coal to Ethylene Glycol and Its Related Technology, Fujian Institute of Research on the Structure of Matter, Chinese Academy of Sciences, Fuzhou 350002, China.*

and viable strategy to optimize the *ZT* value of the SnS compound using the synergetic tuning of temperature and carrier concentration.

Keywords: Thermoelectric material; SnS; synergetic tuning; theoretical study

1. Introduction

Thermoelectric (TE) materials effectively convert heat and electrical energy. To address the current energy challenges and environmental crisis, TE materials have recently attracted increasing interest because they can provide a promising way to collect waste heat energy renewably within industrial processes. The quality of TE materials is usually evaluated by the dimensionless thermoelectric figure of merit ZT ($ZT = S^2\sigma T/\kappa$, where S, σ, T, and κ are the Seebeck coefficient, the electrical conductivity, the absolute temperature, and the thermal conductivity, respectively). Thus, a high S and σ and a low κ are favourable for the materials used as TEs. There is no known upper bound on ZT, but materials that have ZT values higher than unity are rare.[1]

Bi_2Te_3 and PbTe are widely used as TE materials and have ZT ~1. New materials related to PbTe such as PbTe with embedded SrTe nanoparticles give very high values of ZT (> 2)[2] but are not widely used TEs. However, both of these materials face similar challenges due to high costs and the use of toxic elements, particularly lead and tellurium. The price of Te is above 100 dollars per pound and, accordingly, is in limited supply. Conversely, Pb is harmful to human health, and the European Union has regulated its usage in electronic devices. Therefore, low-cost, Earth-abundant and environmentally friendly TE materials are in critical demand for thermal energy conversion. It is necessary to develop high-performance and Pb- and Te-free materials for these applications.

Tin monoselenide SnSe, one of the layered IV-VI semiconductors, has been recently reported as an outstanding TE material because of its ultralow lattice thermal conductivity, particularly when it is arranged in layered slabs. Experimental measurements of a SnSe single crystal point to a record *ZT* of 2.6 at 923 K.[3] These striking results highlight a strategy to discover high-performance TE materials with layered, anisotropic and anharmonic structures, which might lead to exceptionally low lattice thermal conductivities. From this perspective, it seemed worthwhile to study SnSe-type material.[4-6] However, to date, the compound SnS has attracted relatively little attention as a valuable TE system; this may be due to the smaller Seebeck coefficient and higher thermal conductivity that are expected from the lighter SnS compared with SnSe. However, the lattice thermal conductivity of SnS is only 1.7 $W \cdot m^{-1} \cdot K^{-1}$ at 300 K,[7] which is comparable to that of the TE systems that are widely studied (e.g., Bi_2Te_3[8] and $NaCo_2O_4$[9]) and lower than that of the $CoSb_3$[10, 11] system. Another advantage of the SnS compound lies in its Earth-abundant constituent elements (Sn and S); both are also free of any health and environmental hazards.

Most previous studies have investigated the optical properties of SnS,[12-14] but it has not typically been studied as a thermoelectric material.[15-20] Further, most reports have focused on the properties around or below room temperature. Recently, Tan *et al.*[19] found that the *ZT* value for pure SnS was 0.16 at 823 K and that the thermal conductivity (κ) decreased when the temperature rose, which suggested that a larger *ZT* value could be achieved at higher temperatures. More importantly, as the temperature increased further, SnS was observed to

experience a *second-order* phase transition near 878 K where the structure converted from *Pnma* to *Cmcm* symmetry.[21, 22] During this phase transition, the changes involved in the atomic configuration should acutely change the sample density, which could result in enhanced phonon scattering to optimize the thermal conductivity. Additionally, SnS experiences changes in its electronic structure. To date, however, much of the study of this material has been limited to studies in the low-temperature *Pnma* phase. The TE performance in the high-temperature *Cmcm* phase remains significantly unexplored.

Conversely, the *ZT* value of pure SnS is too small to be useful. The key question of SnS as a TE material is that the electrical conductivity of an undoped sample is far too low for TE applications: the largest value measured to date is $\sigma = 10\ \Omega^{-1}\cdot m^{-1}$.[18] Therefore, the improvement of the electrical conductivity is essential to obtain a higher *ZT* in the SnS system. Based on the definition of *ZT*, the conversion efficiency is governed by the working temperature *T* and a series of intrinsic parameters (κ, σ, and *S*). The *ZT* value is proportional to *T* but does not linearly increase with *T* because both σ and *S* are functions of *T*. The typical relation between *ZT* and *T* shows an optimal *T* value where *ZT* reaches its maximum. Similarly, the typical *n*-*ZT* relationship, where *n* is the carrier concentration, shows an optimal carrier concentration where the peak *ZT* is found. Due to such a relationship, the proposed modifications of adjusting both the temperature and carrier concentration provide the opportunity to tune the TE efficiency of SnS. Two recent experimental studies[20, 23] have investigated the potential for such an approach. They showed that the electrical conductivity can be significantly enhanced and that the *ZT* value can

thus be accordingly improved. However, experimental study is only limited to a certain doping element (e.g., elemental Ag in these two experimental studies) and thus cannot produce a universal conclusion; conversely, a theoretical study can accomplish this task. To date, few theoretical studies have predicted the TE properties of SnS and guide experimental efforts. In the theoretical study of Parker and Singh,[24] however, the TE properties of the high-temperature *Cmcm* phase were not evaluated. In addition, the maximum *ZT* achieved by Ag-doped SnS is only moderate (e.g., approximately 0.6).[23] However, it is possible that higher *ZT* values will be attained for the SnS material in the near future. Additionally, the optimal temperature and doping concentration have not been determined experimentally and theoretically. As a result, to improve the *ZT* value, a general understanding of the role of the temperature and doping concentration in the TE properties of SnS is required.

Motivated by the above issues, we performed the first principle computations on the doping and temperature dependence of TE properties of SnS in this study. To explore the influence of the phase transition of SnS, we considered a wide temperature range from 300 to 1080 K. Because SnS melts at near 1153 K and a peritectic reaction occurs near 1133 K,[25] a higher temperature was not attempted. In particular, both *p*- and *n*-doped types were studied. The findings in this study show that cooperatively regulating the carrier concentration in the SnS crystal with temperature can produce a significant improvement in TE performance.

2. Computational details

In the calculations, we use the *Pnma* structure (see Fig. 2a) to calculate the TE properties in the temperature range of 300-800 K, and we use the *Cmcm* structure (see Fig. 2b) for the same purpose in the temperature range of 900-1080 K. The structural and electronic properties of SnS are calculated *via* a plane-wave pseudopotential formulation within the framework of density functional theory (DFT). The code is implemented in the Vienna *ab inito* Simulation Package (VASP).[26] The projector-augmented wave (PAW)[27] potentials are used to describe the interaction between electrons and ions. The generalized gradient approximation (GGA)[28] in the Perdew-Burke-Ernzerhof (PBE) scheme is used to describe the exchange and correlation function, whereas the valence electrons of the sulphur and tin atoms are considered to be $6(3S^2 3p^4)$ and $14(4d^{10} 5S^2 5p^2)$, respectively. In fact, we also considered the HSE06[29] functional and found in this case the band gap of *Pnma* phase is in a larger deviation from the experimental values[30, 31]. Recently, a modification to the semilocal Becke-Johnson potential[32] was proposed. This MBJ potential is useful to better describe the DFT eigenvalues but structure optimization is not ye possible[33]. Before calculations were performed, *k*-point sampling and kinetic-energy cutoff convergence for both the *Pnma* and *Cmcm* structures were tested. Based on the results of the convergence test, a kinetic-energy cutoff of 450 eV and 6×9×9 (9×6×9) Monkhorst-Pack k-points were used for the *Pnma* (*Cmcm*) phase. The total energy converges to 1.0×10^{-4} eV/atom, while and Hellman-Feynman force is smaller than 0.01 eV/Å in the optimized structure. Using the proposed method, the optimized cell parameters were determined to be

a=11.46 Å, *b*=8.06 Å, and *c*=8.86 Å (*a*=8.24 Å, *b*=11.83 Å, and *c*=8.23 Å) for the *Pnma* (*Cmcm*) structures, which are in reasonable agreement with the literature.[30]

The transport calculations require a much finer sampling; therefore, a *k*-point mesh of 12×18×18 (18×12×18) for the *Pnma* (*Cmcm*) phase was used to obtain the electronic band structures and thermal transport parameters. To confirm the validity of these *k*-point meshes, we calculated the transport coefficients of the *Pnma* phase using a different mesh with 10×15×15, 12×18×18, and 14×21×21, respectively. At $p = 1\times10^{19}$ cm^{-3}, the calculated Seebeck coefficient as a function of temperature is shown in Fig. 1, which clearly shows that the calculated Seebeck coefficient converges with the 12×18×18 mesh.

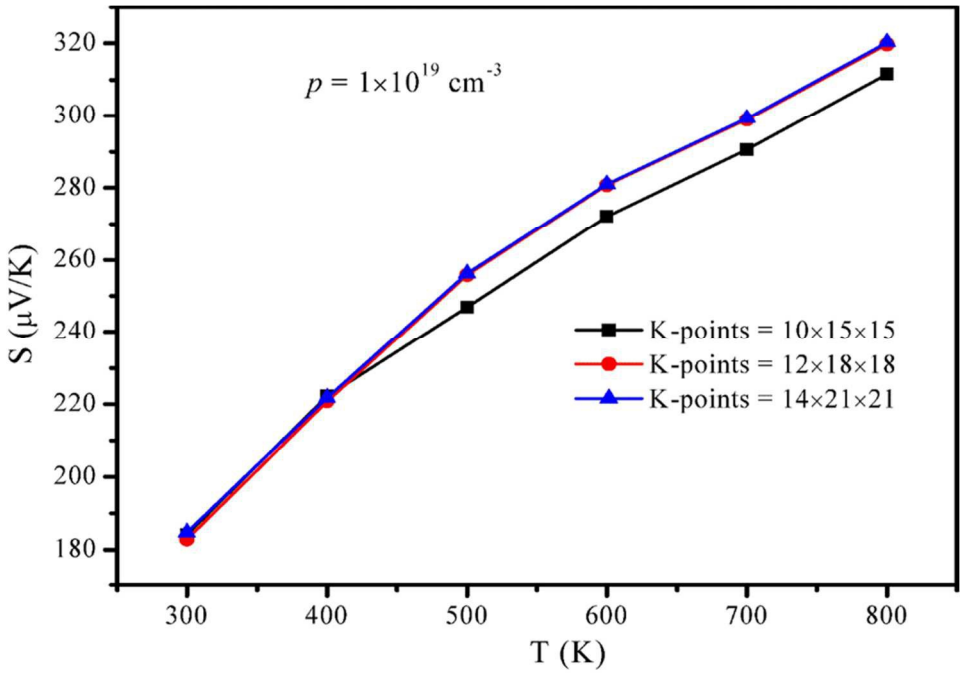

Fig. 1 Seebeck coefficient versus temperature for the *Pnma* phase with different *k*-point grids.

Based on the energy band structures, several TE properties, such as the Seebeck coefficient (*S*), the electrical conductivity (σ) and the electrical thermal conductivity (κ_e), can be derived using the semi-classical Boltzmann transport theory, as implemented in the BOLTZTRAP code.[34] The more detailed information can be seen in the supplementary section. In this package, the grid of *T* is defined by *Tmax* in the input file. Note that the rigid band approximation (RBA) and the constant relaxation time approximation were used to calculate *S* and σ in the above method. In RBA, it is assumed that the band structure of the host is unchanged by doping. RBA usually overestimates the Seebeck coefficient and the power factor,[35] and also, the relaxation time in general depends on the energy and temperature.[36, 37] It is difficult to reliably predict the temperature dependence of transport coefficients using the constant relaxation time approximation. However, a full *E*- and *T*-dependence study of τ using *ab initio* band structure calculations even in simple semiconductors is not currently feasible. Typically, τ is treated as a constant for simplicity and convenience.[38-41]

3. Results and discussion

3.1 Crystal structures of SnS

Fig. 2a shows the SnS crystal in its *Pnma* phase, which exhibits a layered orthorhombic structure with zigzagged atomic chains, in which each Sn atom is bound to two S atoms in the *b*-*c* plane and one additional S atom at a short distance along the *a* axis (i.e., 2+1 coordination). The corresponding bond lengths are 2.69 and 2.65 Å, respectively. The layers pile up with a weak

van der Waals (VDW)-like coupling along the *a* axis. At a high temperature near 878 K, SnS undergoes a *second-order* displacive phase transition to a five-fold coordinated *Cmcm* phase with a higher symmetry (Fig. 2b). In the *Cmcm* phase, the atoms form double layers similar to those in the *Pnma* phase, but they are stacked along the *b* axis. Additionally, each atom is now coordinated to four neighbouring atoms at an equal distance (e.g., 2.93 Å) in the *a*-*c* plane and one additional atom at a short distance (e.g., 2.60 Å) along the *b* axis (i.e., 4+1 coordination). The lengths of the Sn-S bonds parallel to the slab layers, and the distances between the layers are approximately 3 Å, which is suggestive of weak bonding and hence soft phonons, which in turn are favourable for TE performance.

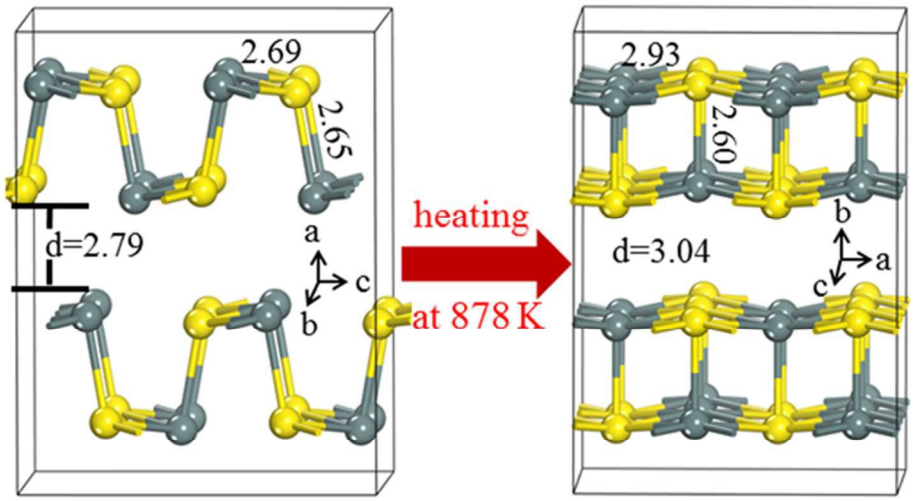

Fig. 2 Crystal structures of SnS in (a) the *Pnma* phase and (b) the *Cmcm* phase. The unit of interatomic distance is in Å. Colour designations: Sn (grey) and S (yellow).

3.2 Electronic band structures

The TE properties of crystalline materials are determined by their band structures. Therefore, we calculated the band structures of SnS within the *Pnma* and *Cmcm* phases; these results are shown in Fig. 3. In this figure, *G, Z, T, Y, S, X, U, R* describe the (0 0 0), (0 0 1/2), (-1/2 0 1/2), (-1/2 0 0), (-1/2 1/2, 0), (0 1/2 0), (0 1/2 1/2), (-1/2 1/2 1/2) high-symmetry points, respectively. For both the *Pnma* and *Cmcm* phases, the conduction band minimum (CBM) is located at point *G*, and the valence band maximum (VBM) lies along the *G-Z* line, which results in an indirect band gap. The band gap is approximately 1.09 eV for the *Pnma* phase and 0.42 eV for the *Cmcm* phase; these values agree with the previously reported theoretical and experimental results,[12, 30, 42-44] which vary in the range of 1.07-1.11 eV in the *Pnma* phase and are equal to 0.3±0.1 eV in the *Cmcm* phase. The significantly smaller band gap in the *Cmcm* phase suggests that the bipolar conduction process occurs at high temperatures.

Because the transport properties are closely related to the electronic states near the highest valence band (HVB) and the lowest conduction band (LCB) for *p*- and *n*-type compounds, respectively, it is reasonable to focus on the energy range near the band gap. The valence and conduction bands are shown to have different characters: the heavy bands near the HVB contribute a high thermopower but exhibit a smaller carrier mobility, whereas the light bands near the LCB are expected to have a higher conductivity. We therefore anticipate different TE behaviours for *p*- and *n*-type doped materials. Further analysis of Figs. 3a and 3b shows that the bandwidths of both the HVB and LCB become larger when changing from the *Pnma* phase (0.65

eV for the HVB and 1.05 eV for the LCB, respectively) to the *Cmcm* phase (0.87 and 1.41 eV, respectively). Therefore, it is suggested that at the *Pnma*-*Cmcm* phase transition, there may be an enhancement of the conductivity.

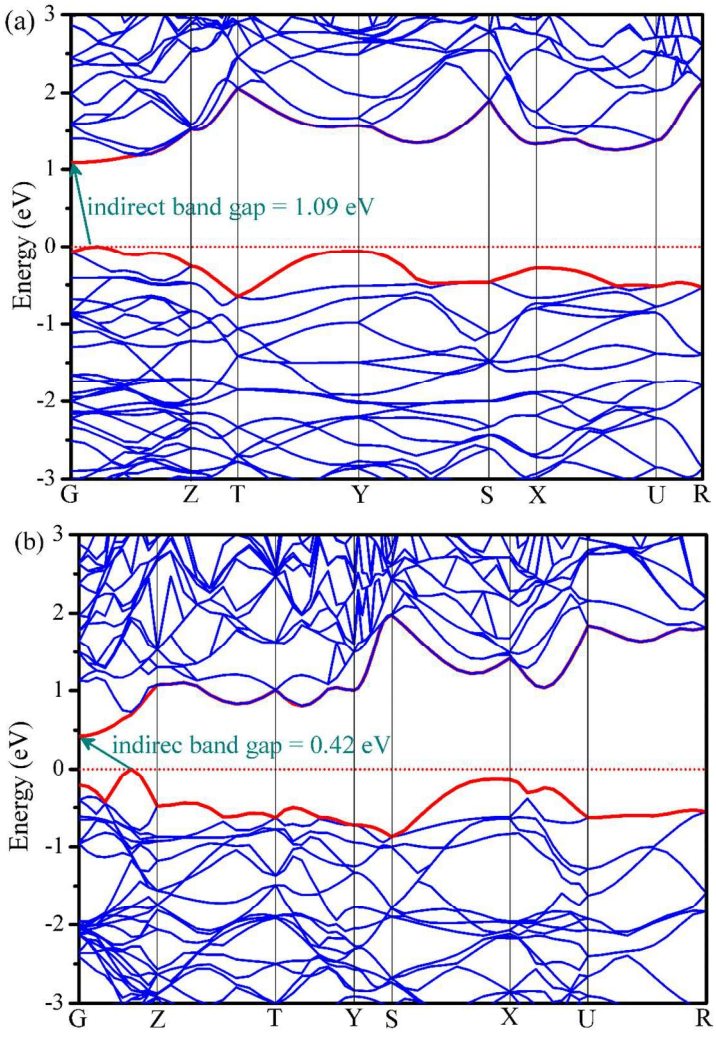

Fig. 3 Band structures of SnS in the *Pnma* (a) and *Cmcm* (b) phases. The energy zero is set to the valence-band maximum. The highest valence band and the lowest conduction band are highlighted in red.

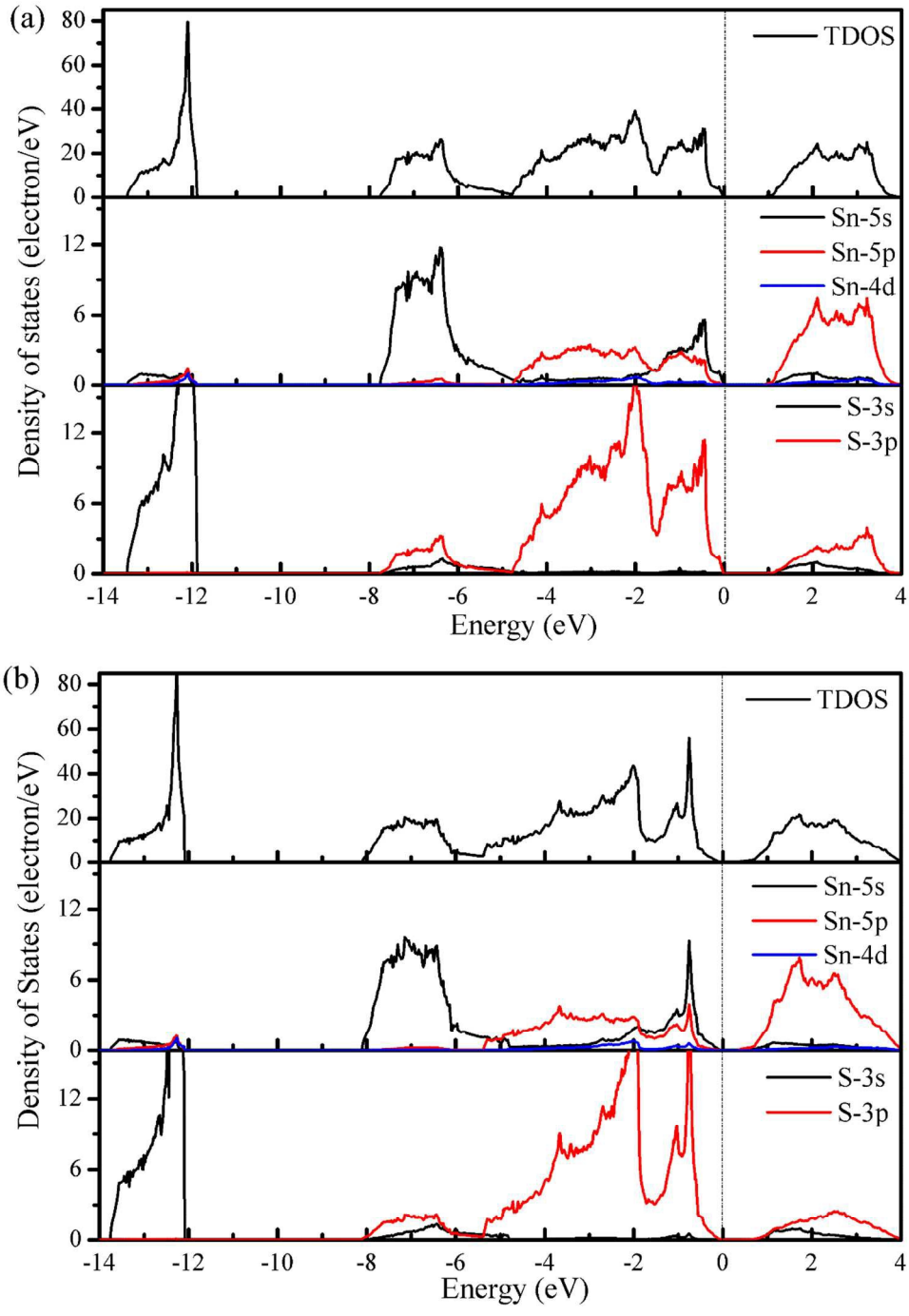

Fig. 4 Total and partial densities of state for SnS within the *Pnma* (a) and *Cmcm* (b) structures. The energy zero is set to the VBM.

Considering the calculated densities of state (DOS) in Fig. 4, we note that the 3*s* states of S are deep and separated from the other valence band states by a gap of approximately 4 eV, which indicates a strong lone electron pair character. The valence bands are formed primarily of the 5s and 5p states of Sn and the 3p states of S, whereas the conduction bands are primarily from the 5p and 3p states of Sn and S, respectively. Additionally, the valence band states from -4.7 to -1.4 eV are responsible for the strong Sn-S covalent bonds that are parallel to the slab layers, whereas those states from -1.4 to 0 eV contribute to the strong covalent bonds that are perpendicular to the slab layers.[30]

Generally, materials with large Seebeck coefficients are usually associated with a large DOS near the band gap.[45] The DOS plotted in Fig. 4 shows that the change in the height of the total DOS is not significant when going from the *Pnma* phase to the *Cmcm* phase; no apparent difference can be observed in the Seebeck coefficient between the *Pnma* and *Cmcm* phases. However, the HVB shows a higher DOS peak than the LCB, which is indicative of a higher Seebeck coefficient for *p*-type doping.

3.3 Thermoelectric properties

The transport properties calculated as a function of the carrier concentration from 300 to 1080 K are shown in Fig. 5. The calculated Seebeck coefficient (*S*) [Fig. 5(a1 and a2)] for both *p*- and *n*-type doped crystals are shown to be sensitive to the carrier concentration. *S* shows a near-linear increase as the carrier concentration decreases in the 300-800 K temperature range.

As mentioned above, the calculated band gap for the *Cmcm* phase is 0.42 eV and thus likely leads to the bipolar effect (i.e., a decrease in the Seebeck coefficient with decreasing carrier concentration, which is the opposite of the usual situation). At 900-1080 K, bipolar conduction appears in the regime below carrier concentrations of 1.12×10^{19} cm^{-3}; however, they are in a doping range that is significantly lighter than the likely optimal doping ranges, which are given as 4.63-8.01 × 10^{19} cm^{-3} for *p*-type and 12.21-14.02 × 10^{19} cm^{-3} for *n*-type at 900-1080 K (see Table 1). Therefore, the *ZT* value at high temperatures with low doping may be degraded by the bipolar effect; however, this will likely not occur at doping levels above 1.12×10^{19} cm^{-3}. This finding is verified by the following results from Fig. 9(b). In addition, the Seebeck coefficient strongly depends on the temperature, which is discussed below.

The electrical conductivity (σ) is also important and is related to the relaxation time (τ). In this paper, the τ value (7.44×10^{-16} s) from the experimental measurements by Nassary *et al*.[18] has been applied to the *n*-doped system. For the *p*-doped system, τ can be deduced using the 300-K data from Hegde *et al*.[13] The reported experimental electrical resistivity ρ is 1.20 Ω·m at this temperature, and the corresponding carrier concentration is 1.52×10^{15} cm^{-3}, which can be combined with the calculated σ/τ to yield $\tau = 15.1 \times 10^{-16}$ s. The obtained τ is near that used in the Ag-doped SnS systems ($\tau = 30 \times 10^{-16}$ s) [20]. We then calculated σ by $\sigma/\tau \times \tau$. The resulting *p*-type and *n*-type electrical conductivities are shown in Fig. 5(b1 and b2), respectively. It is shown that σ for both doping types substantially increases with increasing carrier concentration. For example, as the carrier concentration increases from 10^{18} to 10^{21} cm^{-3}, σ at 900 K increases

rapidly from 2.05×10^3 to 2.29×10^5 $\Omega^{-1}\cdot m^{-1}$ for *p*-type doping and from 9.67×10^2 to 2.48×10^5 $\Omega^{-1}\cdot m^{-1}$ for *n*-type doping. However, the temperature dependence of the electrical conductivity is shown to be relatively weaker. As shown in Fig. 5(b1 and b2), the electrical conductivity gradually declines with temperature in the low-temperature *Pnma* phase. In the high-temperature *Cmcm* phase, σ shows an increasing trend at low doping but decreases at higher doping levels. The high-temperature conductivity is significantly higher with *p*-type doping but is not significantly higher for *n*-type doping. This can be explained by the band structure: the HVB becomes more dispersed in the *Pnma* phase compared to the *Cmcm* phase (see Fig. 3), which indicates a decreased effective mass of hole carrier and, thus, an increased electrical conductivity for *p*-type doping; however, the LCB changes little in going from the *Pnma* phase to the *Cmcm* phase (see Fig. 3). It indicates that there are no apparent changes in the effective mass of electron carrier and thus in the electrical conductivity for *n*-type doping from the *Pnma* phase to the *Cmcm* phase. σ is also significantly larger than those previously reported for pure SnS (e.g., below 500 $\Omega^{-1}\cdot m^{-1}$);[19] the *S* is marginally lower than those of pure SnS (e.g., 350-750 μV/K). The substantial increase in σ and the slight decrease in *S* could result in a net increase in $S^2\sigma$ (i.e., the power factor or *PF*), which is the numerator in the fractional expression of *ZT*. For example, for pure SnS at 823 K, the maximum power factor is 1.34×10^{-4} W/mK^2; for *p*-doped SnS at 800 K, an improved value of 6.93×10^{-4} W/mK^2 is obtained (Table 1).

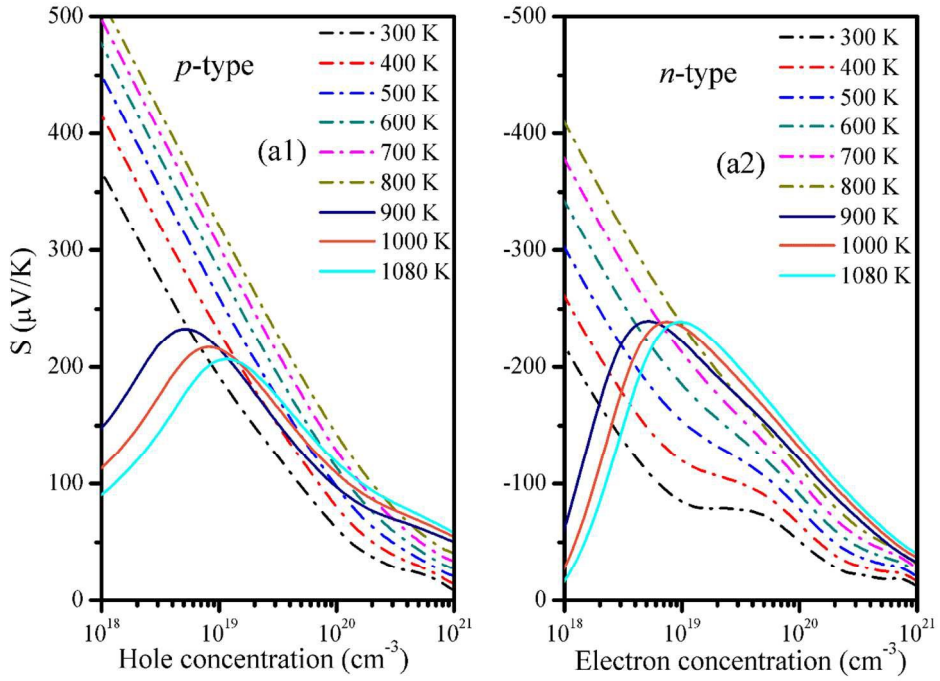

1

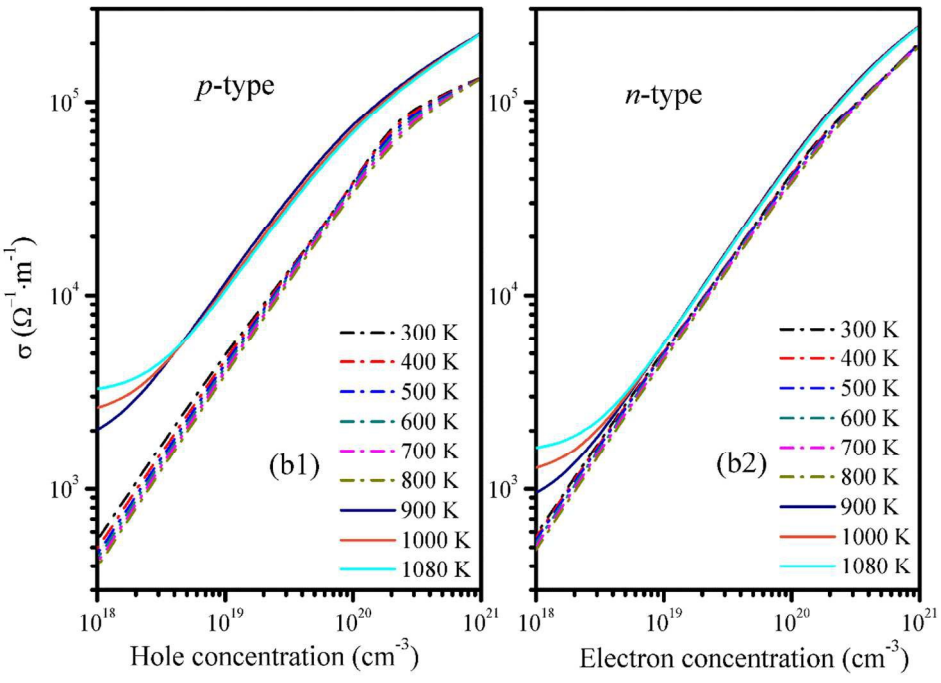

2

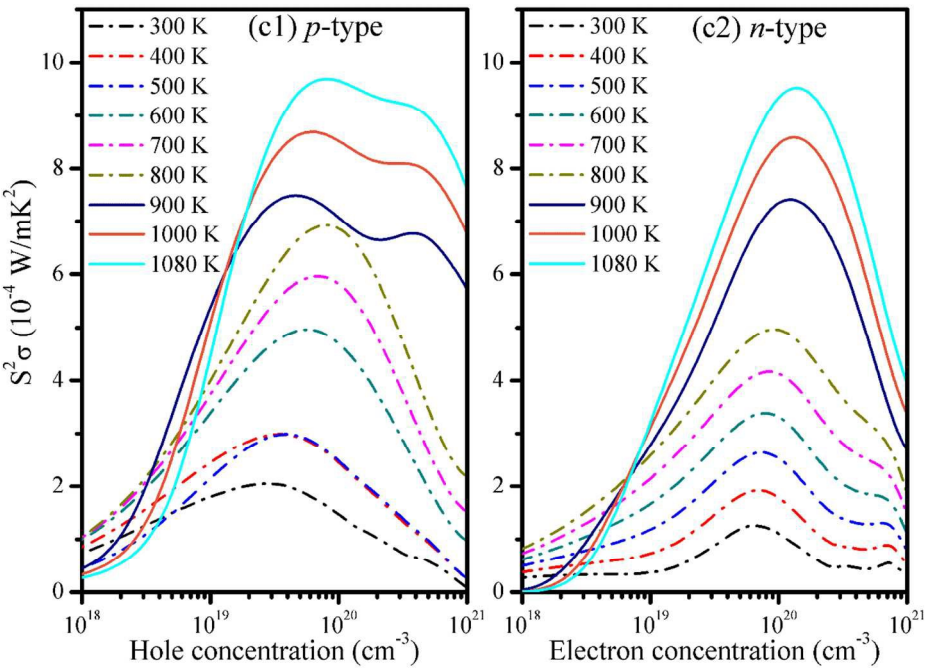

Fig. 5 Transport properties of SnS as a function of the carrier concentration in the temperature range of 300-1080 K: (a1) *p*-type Seebeck coefficients, *S*; (a2) *n*-type Seebeck coefficients, *S*; (b1) *p*-type electrical conductivities, σ; (b2) *n*-type electrical conductivities, σ; (c1) *p*-type power factors, $S^2\sigma$; (c2) *n*-type power factors, $S^2\sigma$.

In TE applications, *PF* ($S^2\sigma$) is an important factor that directly influences TE performance. The *PF* for *p*- and *n*-type materials as a function of the carrier concentration is given in Fig. 5(c1 and c2), respectively. There is an optimal carrier concentration that yields the maximum *PF* (*MPF*). To obtain more detailed information, the optimal carrier concentration, *MPF*, *ZT*, *S*, and σ in the 300-1080 K temperature range are summarized in Table 1. These data indicate that as *T* increases, the *MPF* for both *p*- and *n*-type materials increases, and the optimal carrier concentration for *n*-type doping shifts to a higher level. For *p*-type doping, an increasing trend is

shown at temperatures below 800 K; however, the optimal carrier concentration suddenly decreases at 900 K and then increases again as the temperatures increase above 900 K. At a given temperature, the *n*-type material has a higher optimal carrier concentration than the *p*-type but has lower *MPF* values; this result indicates that *p*-type SnS performs better in terms of TE properties than *n*-type SnS. For *p*-type SnS, the optimal carrier concentration varies from 2.75 to 8.01 × 10^{19} cm^{-3} and thus produces *MPF* values from 2.05 to 9.69 × 10^{-4} $W{\cdot}m^{-1}{\cdot}K^{-2}$. Concurrently, *n*-doped counterparts exhibit *MPF* values from 1.26 to 9.52 × 10^{-4} $W{\cdot}m^{-1}{\cdot}K^{-2}$ with carrier concentrations of 6.68-14.02 × 10^{19} cm^{-3}. Consequently, we predict that SnS will exhibit better TE performance at high temperatures and with heavy doping.

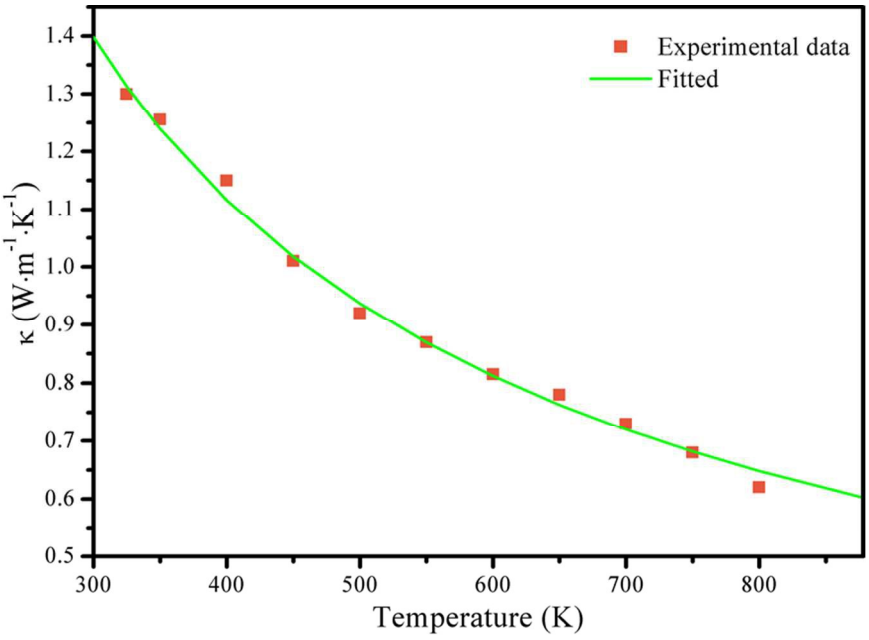

Fig. 6 Thermal conductivity of SnS from Ref. 19 and the fitted curve with the experimental data used in the proposed model, as discussed above.

The thermal conductivity of SnS was investigated from 300 to 800 K by Tan *et al*.[19] They noted that the variations of κ with the doping concentration are weak; thus, it is reasonable to assume that κ is only related to the temperature in this study. The κ values in 300-800 K temperature range are obtained by fitting the experimental data from Tan *et al*.,[19] as shown in Fig. 6. The thermal conductivity is shown to decrease rapidly from 1.40 to 0.65 W/mK as *T* increases from 300 to 800 K. Of note, in the *Cmcm* phase, we set κ as a constant to the fitted value at 800 K (0.65 $W \cdot m^{-1} \cdot K^{-1}$) based on the following facts. For SnSe,[3] κ gradually decreases as the temperatures rise in the *Pnma* phase but changes little in the *Cmcm* phase; the values of κ are also similar near the phase-transition temperature (807 K). For example, the values of κ in $W \cdot m^{-1} \cdot K^{-1}$ along the *c* axis are 0.24, 0.23, 0.22, 0.24 and 0.23 for 675 K, 725 K, 775 K, 825 K, and 875 K, respectively. The biggest difference between these values is smaller than 0.02 $W \cdot m^{-1} \cdot K^{-1}$. SnS shows a similar structure to that of SnSe; therefore, they may have a similar trend in κ. Recently, Tan *et al*.[23] showed that κ in $W \cdot m^{-1} \cdot K^{-1}$ for a SnS-0.5% Ag sample were 0.49, 0.48, 0.44, and 0.46 for 775 K, 825 K, 875 K, and 925 K, respectively, which also indicated that the κ values for SnS are comparable in the neighbouring regimes of the phase transition (phase-transition temperature of SnS is 878 K). Therefore, reasonable *ZT* values for SnS in the *Cmcm* phase could be achieved using the fitted κ value at 800 K (0.65 $W \cdot m^{-1} \cdot K^{-1}$).

Combining the thermal conductivity with the electrical transport coefficients, we finally obtained the dimensionless figure of merit (*ZT*) as a function of the carrier concentration (see Fig. 7). In Fig. 7, it is shown that the *ZT* value can be significantly influenced by both the

temperature and the carrier concentration. For both *p*- and *n*-type doping, the *ZT* value first increases with the carrier concentration, reaches an optimal value, and then decreases; these trends are similar to those found for the power factor. When the temperature rises from 300 to 800 K, the optimal *ZT* value increases from 0.04 to 0.85 for the *p*-type material and from 0.03 to 0.61 for the *n*-type material. With an additional increase in *T*, the optimal *ZT* continues to increase and is shown to be sensitive to temperature; it exceeds unity at 900 K and remains above it, reaching 1.63 for the *p*-type material and 1.59 for the *n*-type material at 1080 K. The strong temperature sensitivity shown makes a TE generator have a longer service life and a higher conversion efficiency in the high-temperature region. Such *ZT*-*T* behaviour in the high-temperature *Cmcm* phase is due to the strong temperature dependence of the Seebeck coefficient (see Fig. 8a). However, a high *ZT* peak value does not always indicate a high efficiency; the average *ZT* value over the imposed working temperature gradient is the critical factor. However, the high-temperature *Cmcm* phase does possess a high average *ZT* value of approximately 1.3 compared with the low-temperature *Pnma* phase (e.g., 0.3±0.05). All of these findings indicate that the high-temperature *Cmcm* phase exhibits good TE performance; thus, this phase should be investigated in more detail. The higher *ZT* at high temperatures is primarily due to the higher electrical conductivity that is present at these temperatures. From Table 1, we also note that at high temperatures, the optimal carrier concentration for the *p*-type material is 4.63-8.01 $\times$ 10^{19} cm^{-3}, which is substantially lower than that for the *n*-type material

(e.g., 12.21-14.02 × 10^{19} cm^{-3}). Such a doping concentration is most likely experimentally controllable for the *p*-type material but is relatively more difficult for the *n*-type material.

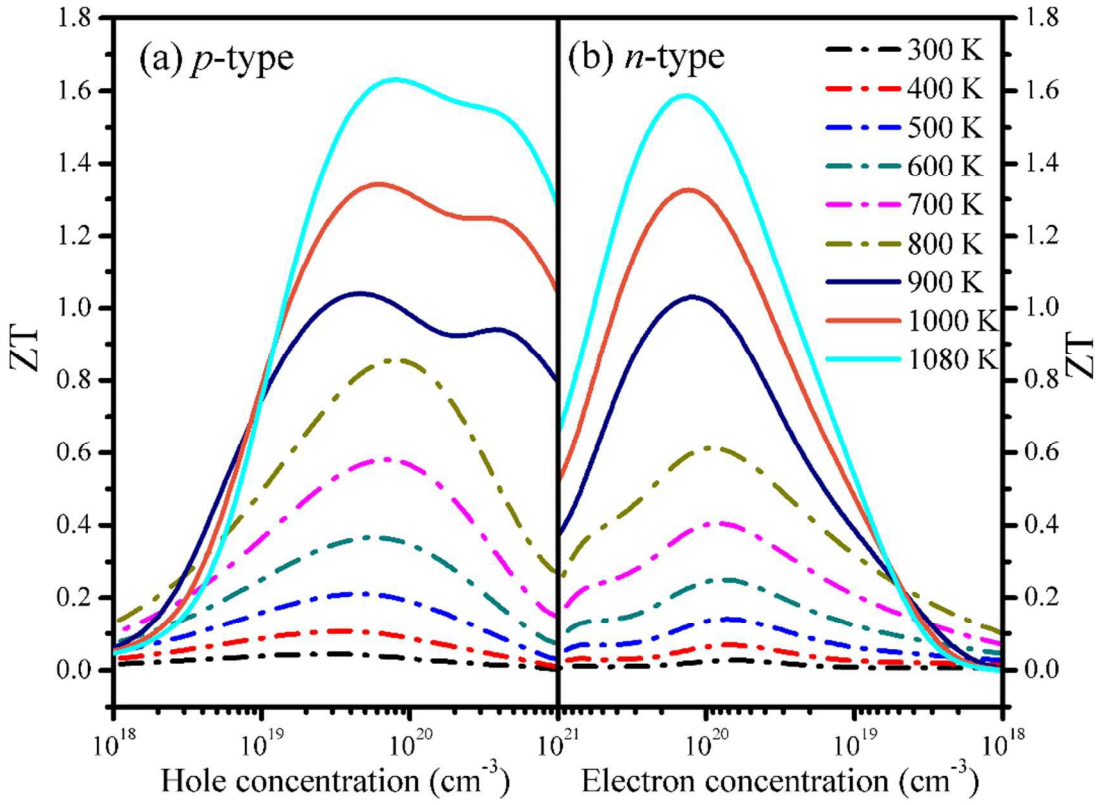

Fig. 7 Calculated *ZT* values as a function of the carrier concentration in the temperature range of 300-1080 K.

Table 1 TE properties of *p*- and *n*-type SnS at optimal carrier concentrations

	p-Type						*n*-Type				
T	P^a	MPF^b	*ZT*	*S*	σ	κ^c	n^a	MPF^b	*ZT*	*S*	σ
300	2.75	2.05	0.04	131.20	1.19	1.40	6.68	1.26	0.03	65.29	2.95
400	3.48	2.98	0.11	143.90	1.44	1.12	7.05	1.92	0.07	79.38	3.05
500	4.66	3.96	0.21	146.17	1.85	0.94	7.50	2.64	0.14	91.15	3.17
600	5.55	4.96	0.37	152.43	2.14	0.81	7.59	3.38	0.25	103.85	3.14
700	7.02	5.96	0.58	152.78	2.57	0.72	8.19	4.16	0.40	112.66	3.28
800	7.79	6.93	0.85	159.64	2.72	0.65	9.33	4.97	0.61	117.74	3.58
900	4.63	7.49	1.04	131.27	4.35	0.65	12.21	7.41	1.03	111.51	5.96
1000	6.36	8.69	1.34	128.86	5.23	0.65	13.39	8.59	1.32	116.53	6.32
1080	8.01	9.69	1.63	127.94	5.92	0.65	14.02	9.52	1.59	121.40	6.46

[a] *p* and *n* are the optimal carrier concentrations for the *p*- and *n*-type materials, respectively. The units for *T*, *p* and *n*, *MPF*, *S*, and σ are K, 10^{19} cm^{-3}, 10^{-4} $W{\cdot}m^{-1}{\cdot}K^{-2}$, $\mu V{\cdot}K^{-1}$, and 10^{4} $\Omega^{-1}{\cdot}m^{-1}$, respectively. [b] *MPF* is the abbreviation of maximum power factor. [c] κ is the thermal conductivity of *p*- and *n*-type doping and the unit is in $W{\cdot}m^{-1}{\cdot}K^{-1}$.

The data presented in this study are now compared with those obtained in previous studies. As stated above, a high *ZT* of 1.61±0.02 for doped-SnS is achieved at 1080 K, which is approximately 10 times as much as the experimental intrinsic value (e.g., 0.16) of pure SnS.[19] This finding indicates that doping and temperature play an important role in improving the *ZT* value of SnS. In particular, at 800 K, the optimal *ZT* value is predicted to be 0.85 (see Table 1) for the *p*-type material in this study, which agrees with that of the previously reported *p*-type SnS (*ZT* = 0.7).[24] Recently, Tan *et al*.[23] reported that a sample of SnS-0.5% Ag has a large *ZT* (0.6 at 923 K), which is smaller than that predicted at high temperatures. The large difference between these values is partially caused by the fact that the carrier concentration of the 0.5% Ag-doped SnS material does not reach the optimum doping level. For example, from 300 to 700 K, the

carrier concentration of SnS-0.5% Ag ranges from 2.72-3 × 10^{18} cm^{-3}, which is smaller by at least an order of magnitude than the predicted optimum doping level (e.g., 2.75-7.02 × 10^{19} cm^{-3}) shown in this study. Those authors also showed that for Ag-doped SnS (see Fig. 3 in Ref. 23), the *ZT* value at a given temperature first increases, then reaches a maximum value at x = 0.5 (x is the Ag content), and finally decreases above x = 0.5 in the *Pnma* phase as Ag doping increases from x = 0 to x = 2. This result indicates that there is an optimum doping level to achieve a peak *ZT* value. The electrical conductivity is shown to increase significantly due to Ag doping, which was also observed by Bera *et al*.[20] These observed trends in *ZT* and σ are consistent with the results of this study. Unfortunately, experiments do not provide the corresponding carrier concentrations for different Ag doping levels at different temperatures; thus, we cannot make a further detailed comparison of these results with those reported in the literatures. In addition, in the context of this study, we observed that the *ZT* value for the high-temperature phase increases faster with temperature, which is in good agreement with the published measurements.

As expected, high *ZT* values can be achieved by cooperative tuning of the doping concentration and temperature. To better understand this synergetic effect, Fig. 8 shows the temperature dependence of the Seebeck coefficient and the *ZT* value for *p*-doped SnS at five different carrier concentrations (e.g., 4 × 10^{17}, 2 × 10^{18}, 2 × 10^{19}, 1 × 10^{20}, and 1 × 10^{21} cm^{-3}). Based on the results reported by Haas and his co-workers [14, 44], the carrier concentration is equal to 4 - 5 × 10^{17} cm^{-3} for an undoped SnS crystal; therefore, we chose 4 × 10^{17} cm^{-3} to

represent the intrinsic behaviour of SnS and thus selected 2×10^{18}, 2×10^{19}, 1×10^{20}, and 1×10^{21} cm^{-3} as four typical doping concentrations to compare with the intrinsic case. At low *T* (e.g., 300-800 K), there is no bipolar effect due to the large band gap; thus, the Seebeck coefficient in Fig. 8a shows an increasing trend in this temperature region, which is typical for a semiconductor. As the temperature increases further (e.g., 900-1080 K), minority carriers arise due to thermal excitation and the coexistence of majority and minority carriers leads to the so-called bipolar effect, which results in a decreasing trend in *S* at high *T* and below $p = 1.12 \times 10^{19}$ cm^{-3}. For example, at $p = 2 \times 10^{18}$ cm^{-3}, the Seebeck coefficient drops from 193.13 to 88.59 μV/K when the temperature changes from 900 to 1080 K. At $p = 1.12 \times 10^{19}$ cm^{-3} and above, the Seebeck coefficient does not enter the bipolar regime and thus exhibits the same trend as the low-temperature phase, which is favourable for the improvement of the *ZT* value in this carrier concentration regime. In Fig. 8b, at $p = 4 \times 10^{17}$ cm^{-3}, the *ZT* value first increases with increasing *T*, and when *T* exceeds 800 K, *ZT* begins to drop due to bipolar conduction. In particular, the *ZT* value is low (e.g., less than 0.1); this indicates that undoped SnS is not a good TE material, even at high temperatures. At $p = 2 \times 10^{18}$ cm^{-3}, there are no apparent changes in the *ZT* value compared to pure SnS. At $p = 2 \times 10^{19}$ cm^{-3} and above, the *ZT* value shows an overall increase as temperature increase. When *T* exceeds 800 K, the *ZT* value increases even faster with temperature; for example, the *ZT* value at $p = 1 \times 10^{20}$ cm^{-3} increases significantly from 0.84 for 800 K to 1.62 for 1080 K. This finding strongly suggests that the high-temperature *Cmcm* phase does not exhibit a better *ZT* value at low doping but does at higher doping. However, this does

not mean that higher doping produces a better *ZT* value; for example, at $p = 1\times10^{21}$ cm^{-3}, the observed *ZT* values are lower than those at $p = 1\times10^{20}$ cm^{-3}. All of the abovementioned results undoubtedly show that the synergetic effect of the carrier concentration and temperature is important to obtain high *ZT* values in SnS crystals.

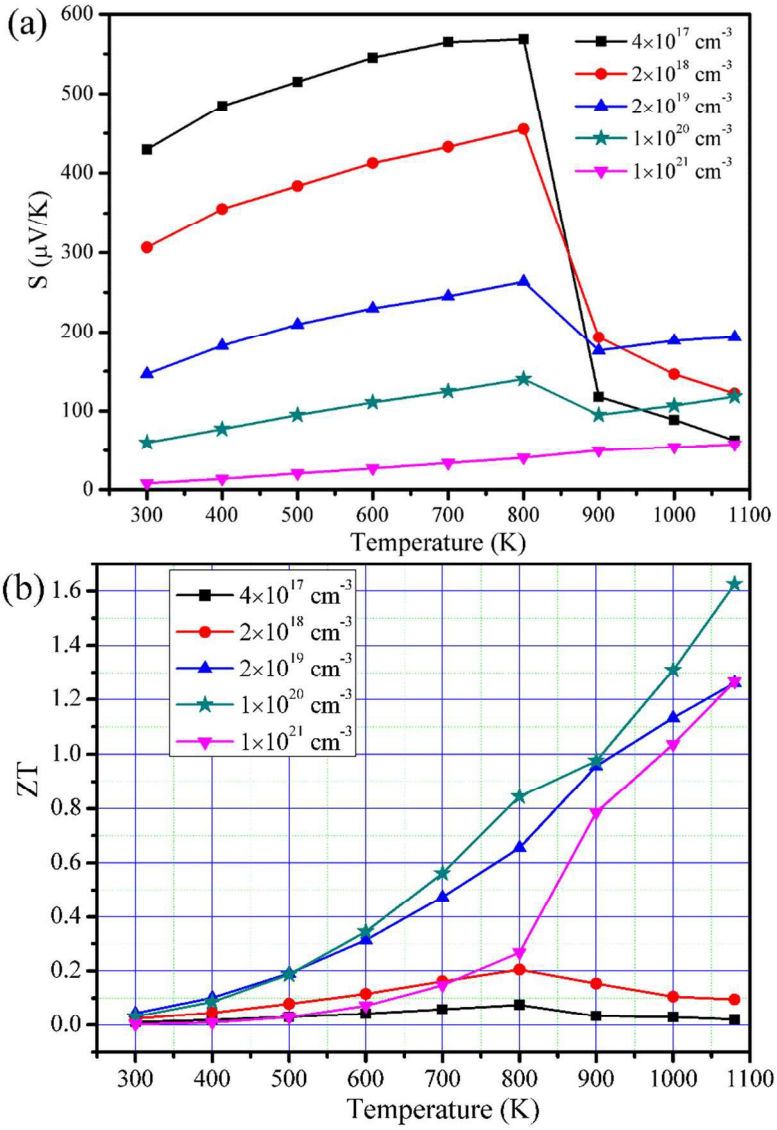

Fig. 8 Temperature dependence of the Seebeck coefficient (a) and the *ZT* value (b) at various *p*-type doping levels.

4. Conclusions

In summary, we have investigated the structural, electronic, and *p*- and *n*-type doped TE properties of SnS across the *Pnma*-*Cmcm* phase transition. An indirect bandgap is found at 1.09 eV and 0.42 eV for the *Pnma* and the *Cmcm* phases, respectively, and the significantly smaller bandgap in the *Cmcm* phase leads to the bipolar effect. In particular, the results of this study show that pure SnS does not exhibit good TE performance, even in the high-temperature *Cmcm* phase; this is significantly different from the case of pure SnSe, in which a higher *ZT* was found in the high-temperature phase. However, we can also obtain a superior *ZT* value in SnS crystal through the cooperative tuning of the carrier concentration and temperature. The optimum doping concentration is predicted to be (2.75-8.01) × 10^{19} cm^{-3} (*p*-type) and (6.68-14.02) × 10^{19} cm^{-3} (*n*-type) in the temperature range of 300-1080 K, which should be accessible for *p*-type but relatively more difficult for *n*-type. Under the optimal doping concentration, the peak *ZT* for the high-temperature phase remains above unity and reaches 1.63 (*p*-type) and 1.59 (*n*-type) at 1080 K, which is approximately 10 times larger than the maximum measured value of pure SnS. Conversely, the low-temperature phase exhibits a *ZT* of less than 1. Additionally, the average *ZT* at low temperatures (e.g., 0.31±0.05) is much lower than that at high temperatures (e.g., approximately 1.3). These facts indicate that SnS might be modified to be a potential high-temperature TE material. Additionally, these findings tell us that the high-temperature *Cmcm* phase of SnS should be studied in more detail. The high *ZT* in doped SnS can be

attributed to its enhanced electrical conductivity. The calculated results reported in this study should be helpful in understanding the TE behaviour of other *IV-VI* group compound systems.

Acknowledgments

This work was supported by the China Postdoctoral Science Foundation (2014M551848), the NSFC project (No: 91122015 and 21303025), Guangxi Natural Science Foundation of China (2014GXNSFBA118029), and the Foundation of the Key Laboratory of Coal to Ethylene Glycol and Its Related Technology of Chinese Academy of Sciences (201401).

Notes and references

1 G. J. Snyder and E. S. Toberer, *Nat Mater*, 2008, **7**, 105.

2 K. Biswas, J. He, I. D. Blum, C. I. Wu, T. P. Hogan, D. N. Seidman, V. P. Dravid and M. G. Kanatzidis, *Nature*, 2012, **489**, 414.

3 L. D. Zhao, S. H. Lo, Y. Zhang, H. Sun, G. Tan, C. Uher, C. Wolverton, V. P. Dravid and M. G. Kanatzidis, *Nature*, 2014, **508**, 373.

4 S. Sassi, C. Candolfi, J. B. Vaney, V. Ohorodniichuk, P. Masschelein, A. Dauscher and B. Lenoir, *Appl Phys Lett*, 2014, **104**, 212105.

5 C. L. Chen, H. Wang, Y. Y. Chen, T. Day and J. Snyder, *J Mater Chem A*, 2014, **2**, 11171.

6 J. Carrete, N. Mingo and S. Curtarolo, *Appl Phys Lett*, 2014, **105**, 101907.

7 D. P. Spitzer, *J Phys Chem Solids*, 1970, **31**, 19.

8 H. J. Goldsmid, *Proc Phys Soc B*, 1956, **69**, 203.

9 K. Takahata, Y. Iguchi, D. Tanaka, T. Itoh and I. Terasaki, *Phys Rev B*, 2000, **61**, 12551.

10 T. Caillat, A. Borshchevsky and J. P. Fleurial, *J Appl Phys*, 1996, **80**, 4442.

11 Y. Kawaharada, K. Kurosaki, M. Uno and S. Yamanaka, *J Alloy Compd*, 2001, **315**, 193.

12 J. Vidal, S. Lany, M. d'Avezac, A. Zunger, A. Zakutayev, J. Francis and J. Tate, *Appl Phys Lett*, 2012, **100**, 032104.

13 S. S. Hegde, A. G. Kunjomana, K. A. Chandrasekharan, K. Ramesh and M. Prashantha, *Physica B*, 2011, **406**, 1143.

14 C. Haas and M. M. G. Corbey, *J Phys Chem Solids*, 1961, **20**, 197.

15 Y. Jayasree, U. Chalapathi, P. Uday Bhaskar and S. R. V, *Appl Surf Sci*, 2012, **258**, 2732.

16 T. H. Patel, R. Vaidya and S. G. Patel, *High Pressure Res*, 2003, **23**, 417.

17 B. Nariya, A. Dasadia, M. Bhayani, A. Patel and A. Jani, *Chalcogenide Lett*, 2009, **6**, 549.

18 M. M. Nassary, *J Alloy Compd*, 2005, **398**, 21.

19 Q. Tan and J. F. Li, *J Electron Mater*, 2014, **43**, 2435.

20 C. Bera, S. Jacob, I. Opahle, N. S. H. Gunda, R. Chmielowski, G. Dennler and G. K. H. Madsen, *Phys Chem Chem Phys*, 2014, **16**, 19894.

21 T. Chattopadhyay, A. Werner, H. G. von Schnering and J. Pannetier, *Revue Phys Appl*, 1984, **19**, 807.

22 T. Chattopadhyay, J. Pannetier and H. G. Von Schnering, *J Phys Chem Solids*, 1986, **47**, 879.

23 Q. Tan, L. D. Zhao, J. F. Li, C. F. Wu, T. R. Wei, Z. B. Xing and M. G. Kanatzidis, *J Mater Chem A*, 2014, **2**, 17302.

24 D. Parker and D. J. Singh, *J Appl Phys*, 2010, **108**, 083712.

25 D. I. Bletskan, *J Ovonic Res*, 2005, **1**, 47.

26 G. Kresse and J. Furthmüller, *Phys Rev B*, 1996, **54**, 11169.

27 P. E. Blöchl, *Phys Rev B*, 1994, **50**, 17953.

28 J. P. Perdew, K. Burke and M. Ernzerhof, *Phys Rev Lett*, 1996, **77**, 3865.

29 J. Heyd, G. E. Scuseria and M. Ernzerhof, *J Chem Phys*, 2003, **118**, 8207.

30 A. Ettema, R. de Groot, C. Haas and T. Turner, *Phys Rev B*, 1992, **46**, 7363.

31 J. M. Chamberlain and M. Merdan, *J Phys C: Solid State Phys*, 1977, **10**, L571.

32 A. D. Becke and E. R. Johnson, *J Chem Phys*, 2006, **124**, 221101.

33 M. César, Y. Ke, W. Ji, H. Guo and Z. Mi, *Appl Phys Lett*, 2011, **98**, 2107.

34 G. K. H. Madsen and D. J. Singh, *Comput Phys Commun*, 2006, **175**, 67.

35 M.-S. Lee and S. D. Mahanti, *Phys Rev B*, 2012, **85**, 165149.

36 S. Ahmad and S. D. Mahanti, *Phys Rev B*, 2010, **81**, 165203.

37 B.-L. Huang and M. Kaviany, *Phys Rev B*, 2008, **77**, 125209.

38 C. Wang, Y. Wang, G. Zhang and C. Peng, *J Phys Chem C*, 2013, **117**, 21037.

39 P. Lu, C. Wu, Y. Li, Z. Yu, H. Cao, T. Gao and S. Wang, *J Mater Sci*, 2013, **48**, 4999.

40 V. K. Gudelli, V. Kanchana, S. Appalakondaiah, G. Vaitheeswaran and M. C. Valsakumar, *J Phys Chem C*, 2013, **117**, 21120.

41 Y. Wang, X. Chen, T. Cui, Y. Niu, Y. Wang, M. Wang, Y. Ma and G. Zou, *Phys Rev B*, 2007, **76**, 155127.

42 L. A. Burton, D. Colombara, R. D. Abellon, F. C. Grozema, L. M. Peter, T. J. Savenije, G. Dennler and A. Walsh, *Chem Mater*, 2013, **25**, 4908.

43 F. Ke, J. Yang, C. Liu, Q. Wang, Y. Li, J. Zhang, L. Wu, X. Zhang, Y. Han, B. Wu, Y. Ma and C. Gao, *J Phys Chem C*, 2013, **117**, 6033.

44 W. Albers, C. Haas and F. van der Maesen, *J Phys Chem Solids*, 1960, **15**, 306.

45 X. Gao, K. Uehara, D. D. Klug, S. Patchkovskii, J. S. Tse and T. M. Tritt, *Phys Rev B*, 2005, **72**, 125202.